Offloading Performance for UAV-aided NOMA-MEC with WPT-enabled for IoT Networks

Gia-Huy Nguyen
ICT Department
FPT University
Hanoi 10000, Vietnam
huynghe180064@fpt.edu.vn

Anh-Nhat Nguyen
ICT Department
FPT University
Hanoi 10000, Vietnam
nhatna3@fe.edu.vn

Tung-Son Ngo
ICT Department
FPT University
Hanoi 10000, Vietnam
sonnt69@fe.edu.vn

Ngoc-Anh Bui
ICT Department
FPT University
Hanoi 10000, Vietnam
anhbn5@fe.edu.vn

Phuong-Chi Le
ICT Department
FPT University
Hanoi 10000, Vietnam
chilp2@fe.edu.vn

Manh-Duc Hoang
ICT Department
FPT University
Hanoi 10000, Vietnam
duchm29@fe.edu.vn

***Abstract*—This article investigates the offloading performance of an unmanned aerial vehicle (UAV)-aided nonorthogonal multiple access (NOMA) incorporating mobile-edge computing (MEC) with the wireless power transfer (WPT)-enabled in Internet of Things (IoT) networks. To assess the system efficacy, we derive the closed-formed expressions of outage successful computation probability (OSCP) under Nakagami-m fading channel. Subsequently, we formulate a system optimization problem of maximizing OSCP by utilizing particle swarm optimization (PSO) algorithm. Numerical findings are implemented with a variety of parameters, thereby validating the precision of our work.**

***Index Terms*—internet of things, unmanned aerial vehicle, non-orthogonal multiple access, wireless power transfer, radio frequency energy harvesting, mobile edge computing**

I. Introduction

The continuous proliferation of the Internet of Things (IoT) devices has significant implications on various domains, particularly with the advent of virtual reality and augmented reality [1]. However, the massive amount of data generated by these devices poses significant challenges on the development of the deep transmission coverage with high reliability. Furthermore, the signal interference caused by a numerous number of high buildings in the dense-urban areas can lead to the degradation of data throughput [2].

To address those deficiencies, unmanned aerial vehicle (UAV) has emerged as a feasible solution with the potential to significantly expand the coverage of IoT networks [3]. Its exceptional mobility and flexible deployment facilitates the communication services between the sever and multiple IoT devices (IDs) with cost-effective services. A key advantage of UAV lies in the ability to establish the Line-of-Sight (LoS) connections with IDs, fostering several benefits such as the better communication channel quality, and reliable network performance [4]. Nevertheless, the UAV and IDs are power-constrained and low computation capability, which is impossible for those devices to execute applications with their available resources.

Hence, the deployment of wireless power transfer (WPT) and mobile-edge computing (MEC) have been presented as compelling solutions for the IoT network [5]. The key feature of MEC severs is to bring the computing resources in the proximity of the network edge, enabling IDs to offload tasks for computation handling [6]. As for the charging part, the WPT is a promising technique to provide the cost-effective energy supplies to the power-constrained IDs. With the help of energy harvesting (EH) technology, the IDs can harvest the broadcast signal to empower themselves. In addition, the association of WPT with MEC tremendously reduces the overall latency, and power depletion caused by the IoT infrastructure drawbacks.

Furthermore, to improve the spectrum efficiency, nonorthogonal multiple access (NOMA) is emerging as a crucial technique for wireless communications networks [7]. It tackles the on-demand data traffic issues by permitting an enormous number of IDs to simultaneously access at the same frequency band in the power domains. In essence, NOMA has the advantages of transmitting an extraordinarily large amount of data to multiple users within the same time slot by exploiting distinct power levels or priorities [8].

Driven by the preceding discourses, this paper investigates an UAV-aided NOMA-MEC with WPT-enabled in IoT networks. Due to the inherent power constraints, the IDs clusters is assumed to be incapable of independently processing data, and must harvest the radio frequency (RF) power emitted by the UAV before offloading computational tasks to the MEC processor for data calculation. Furthermore, the respective probabilities of LoS and non-LoS (NLoS) between UAV and IDs is also evaluated. The following are the primary contribution of our paper:

- We investigated the offloading performance of an UAV-aided NOMA incorporating MEC under the Nakagami-m fading channel in IoT networks. Accordingly, we presented a time-sequenced four-phased protocol, associ-

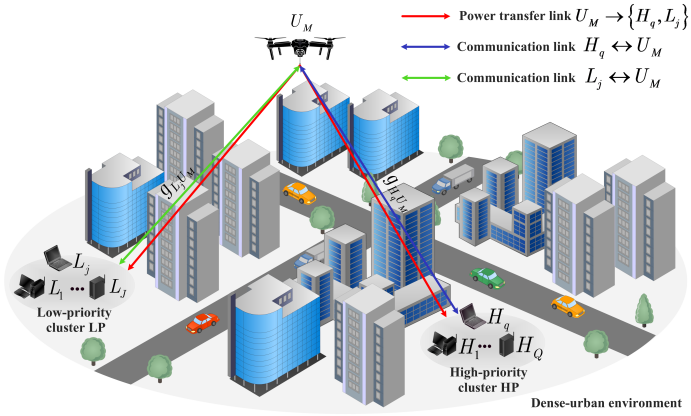

Fig. 1: System model of the UAV-aided WPT-enabled MEC with uplink NOMA in IoT networks.

ated with the best IDs selection (BIS) strategy, designed to guarantee an efficient energy harvesting (EH) and offloading operation.

- To assess the system offloading efficacy, we derived the closed-formed expressions of outage successful computation probability (OSCP) at the BIS of cluster HP (BIH) and BIS of cluster LP (BIL) regarding imperfect channel state information (iCSI) and imperfect successive interference cancellation (iSIC). Moreover, we formulated a system optimization problem of maximizing the OSCP, derived from the PSO algorithm, that determines optimal values for UAV's position and altitude, the EH ratio.
- Numerical findings were implemented with a variety of parameters including UAV's transmit power, the number of IDs in two clusters, the CSI and SIC parameters, the EH ratio and the UAV's position and altitude, thereby validating the precision of our work.

The paper's remaining sections are organized as follows. Section II delves into the characteristics of the system model and communication protocol. Following that, Section III examines the OSCP expressions and optimization problems. Section IV discusses the numerical results that validates the system performance accuracy. The final conclusions are summarized in Section V.

II. System Model and Communication Protocol

A. System and Channel Model

As illustrated in Fig. 1, we present a system model of a dense-urban scenario in the IoT network comprising of an UAV-aided NOMA incorporating a MEC processor, designated as U_M, employed as the calculation station for the high-priority cluster HP with Q devices, designated by H_q, and the low-priority cluster LP with J devices, designated as L_j, where $q \in \{1, ..., Q\}$ and $j \in \{1, ..., J\}$. Specifically, the resource-constrained IDs in two clusters initially harvest RF energy from the broadcast signal emitted by U_M. Subsequently, to facilitate data analysis, the most efficient ID within each cluster is strategically selected to offload computational tasks to the U_M via uplink NOMA. All devices within the system are assumed to possess a single antenna and operate in a half-duplex mode. Furthermore, it is posited that the IDs are all carrying out identical workloads with length l (bits), and the tasks are independently categorized into discrete groups. Therefore, the offloaded capacity of both clusters is expressed as: $\mathcal{C}_k^{off} = \sigma_k l$, where σ_k represents the offloading ratio, with $(0 < \sigma_k < 1)$ and $k \in (q, j)$.

We adopt a 3D Cartesian coordinate system, in which ID clusters severs as the ground nodes, denoted as $H_q\,(x_q, y_q, 0)$ and $L_j\,(x_j, y_j, 0)$, while the UAV's coordinate is represented by $U_M\,(x_U, y_U, h_U)$. Supposing the large-scale fading channel between UAV and ground devices is characterized by the LoS and NLoS probabilistic model. Thus, the mean path-loss is expressed as follows:

$$\overline{\mathcal{L}}_{ab} = \left[\frac{\mathbb{K}^{los} - \mathbb{K}^{nlos}}{1 \;+\; \tau_1 e^{-\tau_2(\varphi_{ab} - \tau_1)}} + \mathbb{K}^{nlos}\right] \mathcal{D}_{ab}^{\theta}, \tag{1}$$

where $ab \in \{H_qU_M, L_jU_M\}$, $\mathbb{K}^{los} = \mu^{los}\left(\frac{c}{4\pi f_c}\right)^{-1}$, $\mathbb{K}^{nlos} = \mu^{nlos}\left(\frac{c}{4\pi f_c}\right)^{-1}$, μ^{los} and μ^{nlos} are the excessive path-losses of LoS and NLoS communications; c and f_c are the speed of light and the carrier frequency, respectively; τ_1 and τ_2 are the parameters that vary depending on the surrounding environments; $\varphi_{ab} = \frac{180}{\pi}\arcsin(\frac{h_U}{\mathcal{D}_{ab}})$ is the elevation angle; $\mathcal{D}_{ab} = \sqrt{(x_b - x_a)^2 + (y_b - y_a)^2 + (h_b - h_a)^2}$ is the distance of ab; θ is the path-loss exponent.

We assume that the channel coefficients g_{ab} are independent, and followed the Nakagami-m distribution. However, due to some practical factors (such as the quantization or feedback latencies), the system model is inevitably affected by the iCSI [10]. Thus, the channel coefficient can be written as: $g_{ab} = \tilde{g}_{ab} + \lambda_{ab}$, where $\tilde{g}_{ab}$ is the estimated channel coefficient, λ_{ab} is the channel estimation error approximated by the additive Gaussian random variable distribution, $\lambda_{ab} \sim \mathcal{CN}(0, \Omega_{ab})$. Within this paper, we assume that the estimation error variance Ω_{ab} is a constant value [9].

Accordingly, by estimating the maximum signal-to-noise ratios (SNRs) of $U_M - H_q$ and $U_M - L_j$ links, the channel gains for the BIS in two clusters are obtained as: $|\tilde{g}_{k^*}|^2 = \max\left\{|\tilde{g}_{\mathbb{I}_{k^*}U_M}|^2\right\}$, where $k^* \in (q^*, j^*)$, and $\mathbb{I} \in (H, L)$. As the channel gains is modelled to be affected by the Nakagami-m distribution, the probability density function (PDF) and cumulative distribution function (CDF) of the channel power gains $|\tilde{g}_{k^*}|^2$ are expressed as:

$$f_{|\tilde{g}_{k^*}|^2}(x) = \ddot{\mathcal{K}} \sum_i (\mathcal{K} - 1)\, x^{m-1+\bar{i}} e^{-\frac{xm}{\xi_{k^*}}(i+1)}, \tag{2}$$

$$F_{|\tilde{g}_{k^*}|^2}(x) = \sum_i (\mathcal{K})\, x^{\bar{i}} e^{-\frac{ixm}{\xi_{k^*}}}, \tag{3}$$

where $\mathcal{K} \in \{Q, J\}$, $i = \{h, t, l, p, a\}$, $\sum_i (\mathcal{K} - 1) = \sum_{i=0}^{\mathcal{K}-1} \Phi_i (-1)^i \Xi_{1,i} \Xi_{2,i}$, $\Phi_i = \sum_{i_1=0}^{i} \sum_{i_2=0}^{i-i_1} \cdots \sum_{i_{m-1}=0}^{i-i_1-i_2-\ldots-i_{m-2}}$,

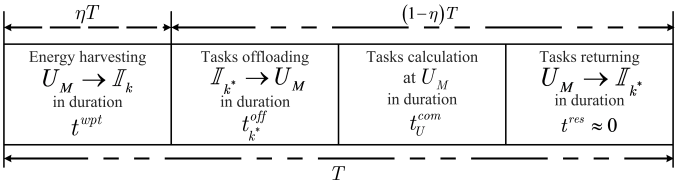

Fig. 2: The time-sequenced protocol for the proposed system.

$\Xi_{1,i} = \binom{\mathcal{K}-1}{i}\binom{i}{i_1}\binom{i-i_1}{i_2}...\binom{i-i_1-i_2...-i_{m-2}}{i_{m-1}}$,
$\Xi_{2,i} = \prod_{s=0}^{m-2}\left[\frac{1}{s!}\left(\frac{m}{\xi_{k^*}}\right)^s\right]^{i_{s+1}}\left[\frac{1}{(m-1)!}\left(\frac{m}{\xi_{k^*}}\right)^{m-1}\right]^{i-...-i_{m-1}}$,
$\ddot{\mathcal{K}} = \frac{\mathcal{K}}{(m-1)!}\left(\frac{m}{\xi_{k^*}}\right)^m$, $\bar{i} = (m-1)(i-i_1) - (m-2)i_2 - ... - i_{m-1}$, $m \in (2,3,4,...)$.

B. Communication Protocol

This subsection presents the time-sequenced four-phased protocol for the proposed system. Depicted in Fig. 2, the protocol flowchart is described as follows:

- In the first phase, denoted as t^{wpt}: U_M transmits the broadcast signal to the ID clusters for EH. Thereafter, the BIH and BIL, denoted as H_{q^*} and L_{j^*}, are selected based on the device that exhibits the maximum SNRs. Thus, the transmitted energy to the IDs can be expressed as: $E_{k^*} = \frac{\beta P_U t^{wpt}\left(|\tilde{g}_{k^*}|^2+\Omega_{k^*}\right)}{\bar{\mathcal{L}}_{k^*}}$, where β is the EH coefficient, with $(0<\beta<1)$; P_U is the power transmission of U_M; $t^{wpt} = \eta T$, where η is the EH ratio, with $(0<\eta<1)$; and T is the transmission block time.
- During the second phase, denoted as $t^{off}_{k^*}$: H_{q^*} and L_{j^*} concurrently offload their tasks via uplink NOMA resulting in the composite signal obtained at U_M as: $y^{MEC}_U = \sqrt{\frac{P_{q^*}}{\bar{\mathcal{L}}_{q^*}}}(\tilde{g}_{q^*}+\lambda_{q^*})x_{q^*} + \sqrt{\frac{P_{j^*}}{\bar{\mathcal{L}}_{j^*}}}(\tilde{g}_{j^*}+\lambda_{j^*})x_{j^*} + n_U$, where $P_{k^*} = \frac{E_{k^*}}{(1-\eta)T - t^{com}_U}$ is the power transmit of the BIS to U_M; x_{k^*} is the transmitted signal of $\mathbb{I}_{k^*}$; $n_U \sim \mathcal{CN}(0,\mathcal{N}_0)$ is subject to the additive white Gaussian noise (AWGN). In the signal decoding stages, U_M initially prioritizes the decoding of x_{q^*} by assuming the remaining signal x_{j^*} to be interference. Subsequently, to tackle with the decoding of x_{j^*}, U_M employs SIC for extracting the previously decoded x_{q^*} signal. Hence, the expressions of the signal-to-interference-plus-noise ratios (SINRs) for x_{q^*} and x_{j^*} is expressed as:

$$\gamma^U_{q^*} = \frac{z_1 x^2}{z_2 y^2 + z_3}, \tag{4}$$

$$\gamma^U_{j^*} = \frac{z_2 y^2}{\psi z_1 x^2 + z_4}, \tag{5}$$

where $z_1 = \frac{\gamma_{q^*}}{\bar{\mathcal{L}}_{q^*}}$, $z_2 = \frac{\gamma_{j^*}}{\bar{\mathcal{L}}_{j^*}}$, $z_3 = z_1\Omega^2_{q^*} + z_2\Omega^2_{j^*} + 1$, $z_4 = \psi z_1\Omega^2_{q^*} + z_2\Omega^2_{j^*} + 1$, $\gamma_{q^*} = \frac{\beta\gamma_U t^{wpt}}{\bar{\mathcal{L}}_{q^*}\left[(1-\eta)T - t^{com}_U\right]}$, $\gamma_{j^*} = \frac{\beta\gamma_U t^{wpt}}{\bar{\mathcal{L}}_{j^*}\left[(1-\eta)T - t^{com}_U\right]}$, $\gamma_U = \frac{P_U}{\mathcal{N}_0}$, $x = |\tilde{g}_{q^*}|^2$, $y = |\tilde{g}_{j^*}|^2$, ψ denotes the residual interference caused by the iSIC, with $(0 \le \psi \le 1)$, and $\psi = 0$ represents the ideal system decoding, namely perfect SIC (pSIC).

- During the third phase, denoted as t^{com}_U: The offloaded tasks undergo calculation at MEC sever. The temporal duration necessary for the completion of these computational processes with a number of task bits is expressed as follows: $t^{com}_U = \frac{\left(\mathcal{C}^{off}_{q^*}+\mathcal{C}^{off}_{j^*}\right)\varpi}{f_{MEC}}$, where ϖ is the number of CPU cycles requires to compute a single task bit and f_{MEC} is the MEC's operating frequency at U_M.
- In the final phase, denoted as t^{res}: U_M transmits the calculated results back to the corresponding BIS within its designated cluster. Notably, due to the minimal energy depletion and brief latency associated with the data retrieval, the t^{res} phase can be considered negligible [2].

III. Performance Analysis

A. Outage successful computation probability (OSCP)

This subsection focuses on deriving the analytical expression for the OSCP of the BIH and BIL, denoted by $\Psi_{\mathcal{K}}$ with $\mathcal{K} \in (Q,J)$. By fusing the outage probability (OP) [9] with the successful computation probability (SCP) [11] expressions, the OSCP is eventually defined as the likelihood that the duration of the offloaded tasks at respective clusters $t^{off}_{k^*}$ accomplishes within the prescribed latency threshold T^{th}, while the instantaneous channel capacity C_{k^*} functions above a predetermined rate $R^{th}_{k^*}$. Thus, the OSCP of the BIH and BIL are expressed as:

$$\Psi_{\mathcal{K}} = \Pr\left\{t^{off}_{k^*} < T^{th}, C_{k^*} > R^{th}_{k^*}\right\}, \tag{6}$$

where $t^{off}_{k^*} = \frac{\mathcal{C}^{off}_{k^*}}{C_{k^*}}$, $C_{k^*} = WT^{th}\log_2\left(1+\gamma^U_{k^*}\right)$, $T^{th} = (1-\eta)T - t^{com}_U$, and W is the bandwidth.

Lemma 1: The closed-form expression for the OSCP of the BIH under Nakagami-m fading channel is given as:

$$\Psi_Q = \left[\vartheta^{(J-1)}_1 - \vartheta^{(Q,J-1)}_2\vartheta^n_Q\right]\left[\vartheta^{(J-1)}_1 - \vartheta^{(Q,J-1)}_3\vartheta^o_Q\right],$$

where $\vartheta^{(J-1)}_1 = \ddot{J}\sum_h(J-1)\Theta_{j^*}$, $\vartheta^{(Q,J-1)}_2 = \frac{\pi\ddot{J}}{2N}\sum_t(Q)\sum_l(J-1)$, $\vartheta^{(Q,J-1)}_3 = \frac{\pi\ddot{J}}{2O}\sum_p(Q)\sum_a(J-1)$, $\vartheta^n_Q = \sum_{n=1}^{N}\Theta^n_Q$, $\vartheta^o_Q = \sum_{o=1}^{O}\Theta^o_Q$, $\Theta_{j^*} = (m-1+\bar{h})!\left(\frac{m(h+1)}{\xi_{j^*}}\right)^{-m-\bar{h}}$,

$$\Theta^n_Q = \sqrt{1-\varphi^2_n}\frac{\left(\Delta^{(\wp_n)}_Q\right)^{\bar{t}}e^{-\frac{tm}{\xi_{q^*}}\Delta^{(\wp_n)}_Q}\wp_n^{m-1+\bar{t}}\omega_n^{\frac{\wp_n^2 m(l+1)}{\xi_{j^*}}-1}}{\ln^2(\omega_n)},$$

$\varphi_n = \cos\left(\frac{\pi(2n-1)}{2N}\right)$, $\Delta^{(\wp_n)}_Q = \sqrt{\frac{\delta_Q(z_2\wp_n^2+z_3)}{z_1}}$, $\wp_n = -\frac{1}{\ln(\omega_n)}$, $\omega_n = \frac{\varphi_n+1}{2}$, $\delta_Q = 2^{\frac{\mathcal{C}^{off}_{q^*}}{W(T^{th})^2}} - 1$,

$$\Theta^o_Q = \sqrt{1-\varphi^2_o}\frac{\left(\phi^{(\wp_o)}_Q\right)^{\bar{p}}e^{-\frac{pm}{\xi_{q^*}}\phi^{(\wp_o)}_Q}\wp_o^{m-1+\bar{a}}\omega_o^{\frac{\wp_o^2 m(a+1)}{\xi_{j^*}}-1}}{\ln^2(\omega_o)},$$

$\varphi_o = \cos\left(\frac{\pi(2o-1)}{2O}\right)$, $\phi^{(\wp_o)}_Q = \sqrt{\frac{\partial_Q(z_2\wp_o^2+z_3)}{z_1}}$, $\wp_o = -\frac{1}{\ln(\omega_o)}$, $\omega_o = \frac{\varphi_o+1}{2}$, $\partial_Q = 2^{\frac{R^{th}_{q^*}}{WT^{th}}} - 1$, N and O *is the complexity-vs-accuracy trade-off coefficient* [13].

Proof 1: See Appendix A.

Lemma 2: The closed-form expression for the OSCP of the BIL under Nakagami-m fading channel is expressed as:

$$\Psi_J = \left[\vartheta_1^{(Q-1)} - \vartheta_2^{(J,Q-1)}\vartheta_J^n\right]\left[\vartheta_1^{(Q-1)} - \vartheta_3^{(J,Q-1)}\vartheta_J^o\right],$$

where $\vartheta_1^{(Q-1)} = \ddot{Q}\sum_h (Q-1)\,\Theta_{q^*}$, $\vartheta_2^{(J,Q-1)} = \frac{\pi\ddot{Q}}{2N}\sum_t (J)\sum_l (Q-1)$, $\vartheta_3^{(J,Q-1)} = \frac{\pi\ddot{Q}}{2O}\sum_p (J)\sum_a (Q-1)$, $\vartheta_J^n = \sum_{n=1}^{N}\Theta_J^n$, $\vartheta_J^o = \sum_{o=1}^{O}\Theta_J^o$, $\Theta_{q^*} = (m-1+\bar{h})!\left(\frac{m(h+1)}{\xi_{q^*}}\right)^{-m-\bar{h}}$,

$$\Theta_J^n = \sqrt{1-\varphi_n^2}\,\frac{\left(\Delta_J^{(\wp_n)}\right)^{\bar{t}} e^{-\frac{tm}{\xi_{j^*}}\Delta_J^{(\wp_n)}} \wp_n^{m-1+\bar{l}}\omega_n \frac{\wp_n^2 m(l+1)}{\xi_{q^*}}-1}{\ln^2(\omega_n)},$$

$\Delta_J^{(\wp_n)} = \sqrt{\frac{\delta_J(\psi z_1\wp_n^2+z_4)}{z_2}}$, $\delta_J = 2^{\frac{c_{j^*}^{off}}{W(T^{th})^2}} - 1$, $\Theta_J^o =$

$$\sqrt{1-\varphi_o^2}\,\frac{\left(\phi_J^{(\wp_o)}\right)^{\bar{p}} e^{-\frac{pm}{\xi_{j^*}}\phi_J^{(\wp_o)}} \wp_o^{m-1+\bar{a}}\omega_o \frac{\wp_o^2 m(a+1)}{\xi_{q^*}}-1}{\ln^2(\omega_o)},\quad \phi_J^{(\wp_o)} =$$

$\sqrt{\frac{\partial_J(\psi z_1\wp_o^2+z_4)}{z_2}}$, and $\partial_J = 2^{\frac{R_{j^*}^{th}}{WT^{th}}} - 1$.

Proof 2: The proof is similar to the *Lemma 1*.

B. Offloading Performance Optimization: Problems and Solution

This subsection proposes a PSO-based solution for maximizing OSCP of the BIH and BIL by determining the most optimal position and altitude of UAV, and the EH ratio designated as $(x_U^*, y_U^*, h_U^*, \eta^*)$. The optimization problems are formulated as follows:

$$\begin{aligned}
\text{(P1):}\quad & \underset{x_U, y_U, h_U, \eta}{\text{maximize}} \quad \Psi_{\mathcal{K}} \\
& \text{subject to} \quad 0 \le x_U \le x_U^{\max}, && \text{(7a)}\\
& \qquad\qquad 0 \le y_U \le y_U^{\max}, && \text{(7b)}\\
& \qquad\qquad 0 \le h_U \le h_U^{\max}, && \text{(7c)}\\
& \qquad\qquad 0 \le \eta \le 1, && \text{(7d)}
\end{aligned}$$

where (7) constraints are the conditions of UAV's position and altitude with the EH ratio. The following is the pseudo-code of **Algorithm 1**: PSO-OSCPMax.

IV. Numerical Results

This section discusses the numerical findings that validates the offloading performance of the aforementioned system. The values for all system parameters of the simulations is specified in the following: $(x_U, y_U) = (0,0)$, $h_U \in (20,100)$ (m), $H_q(60,60,0)$ (m), $L_j(57,57,0)$ (m), $\tau_1 = 0.1139$, $\tau_2 = 12.0870$, $\mu^{los} = 1.6$, $\mu^{nlos} = 23$, $c = 3.10^8$, $f_c = 2.10^5$ (Hz), $W = 2.10^8$ (Hz), $\gamma_U \in (0,20)$ (dB), $\eta \in (0,1)$, $\beta = 0.8$, $T = 1$ (s), $\theta = 2$, $(C_{q^*}^{off}, C_{j^*}^{off}) = (0.6.10^2, 0.4.10^2)$, $f_{MEC} = 10^8$ (Hz), $\varpi = 10^2$, $R_{q^*}^{th} = R_{j^*}^{th} = 400$, $m = 2$, $N = O = 10^2$, $\mathcal{Q} = 100$, $\mathcal{O} = 50$.

Fig. 3 illustrates the impact of the UAV's average transmit power γ_U, with various IDs Q and J, on the OSCP of BIH and BIL. The remarkable alignment of the numerical simulations and the theoretical analysis validates the proposed model's precision. Furthermore, the result indicates that simultaneously increasing the number of devices elevates OSCP. This can be attributed to the expansion of a larger pool of BIS options, as the UAV has the greater flexibility in selecting a device with

Algorithm 1 PSO-OSCPMax

Initialization

Set PSO parameter values: r, α_1, α_2, $\mathcal{Q}$, $\mathcal{O}$

Generate the particle velocities and positions $\mathcal{V}_p$, $\mathcal{X}_p(x_U^*, y_U^*, h_U^*, \eta^*)$

Generate personal and social best positions $\mathcal{P}_p$, $\mathcal{S}_p$

The PSO loops

For p particles of $\mathcal{Q}$ in $\mathcal{O}$ iterations

Randomly generate ν_1^n and ν_2^n in the range of $(0,1)$

Update new position: $\mathcal{X}_p^{n+1} = \mathcal{X}_p^n + \mathcal{V}_p^{n+1}$

Update new velocity: $\mathcal{V}_p^{n+1} = r\mathcal{V}_p^n + \alpha_1\nu_1^n\left(\mathcal{P}_p^n - \mathcal{X}_p^n\right) + \alpha_2\nu_2^n\left(\mathcal{S}_p^n - \mathcal{X}_p^n\right)$

Evaluate the best personal position:

If $\mathcal{F}(\mathcal{X}_p^{n+1}) \ge \mathcal{P}_p^n$ then $\mathcal{P}_p^{n+1} = \mathcal{X}_p^{n+1}$

If $\mathcal{F}(\mathcal{X}_p^{n+1}) < \mathcal{P}_p^n$ then $\mathcal{P}_p^{n+1} = \mathcal{P}_p^n$

Evaluate the best global position:

$\mathcal{S}_p^n = \max\left\{\mathcal{P}_p^n\right\}$

If $\mathcal{F}(\mathcal{X}_p^n) \ge \mathcal{S}_p$ then $\mathcal{S}_p = \mathcal{X}_p^n$

$n \leftarrow n+1$

Return: $\mathcal{F}(\mathcal{S}_p^n)$ as the optimal value of its respective fitness function (Ψ_Q or Ψ_J).

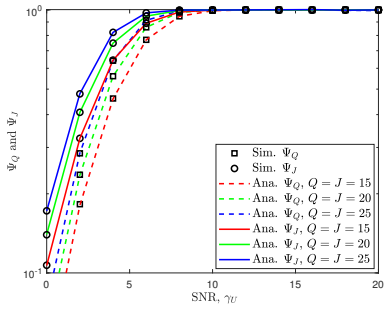

Fig. 3: Impact of the UAV's average transmit SNR γ_U on OSCP of the BIH and BIL with different number of IDs, with $h_U = 50$ (m), $\eta = 0.15$, $\Omega = 3$, and $\psi = 0.4$.

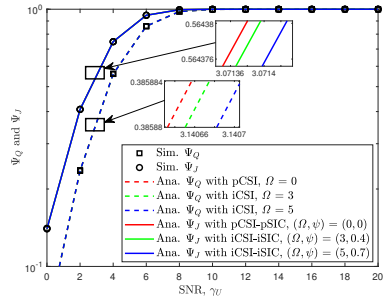

Fig. 4: Impact of the iCSI parameter Ω and iSIC parameter ψ on OSCP of the BIH and BIL, with $Q = J = 20$, $h_U = 50$ (m), and $\eta = 0.15$.

superior capabilities for task offloading. Additionally, a higher transmit SNR contributes to the augmentation of the OSCP, as IDs are provided more power to efficiently offload duties.

Fig. 4 depicts the impact of iCSI and iSIC on the OSCP of the BIH and BIL. As depicts in the figure, the pCSI and pSIC conditions facilitates the maximum system offloading performance. Nevertheless, in practice, this ideal state is extremely challenging to be acquired in dynamic channel environments due to hardware limitations and network connectivity issues. Hence, it is obvious that the augmentation of iCSI-iSIC parameters inevitably results in the degradation of the system offloading efficacy.

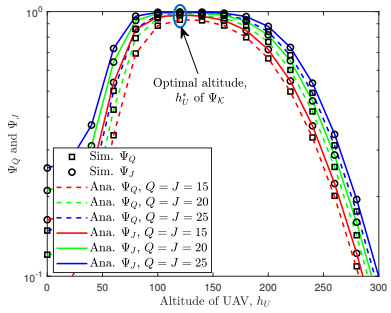

Fig. 5: Impact of the UAV's altitude h_U on OSCP of the BIH and BIL, with $\gamma_U = 4$ (dB), $\eta = 0.1$, $\Omega = 3$, and $\psi = 0.4$.

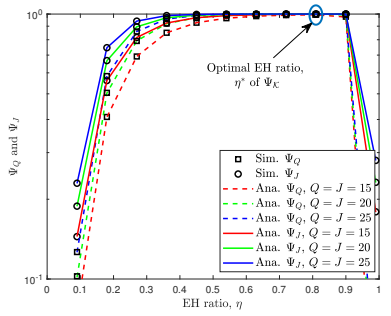

Fig. 6: Impact of the EH ratio η on OSCP of the BIH and BIL, with $\gamma_U = 4$ (dB), $h_U = 30$ (m), $\Omega = 3$, and $\psi = 0.4$.

Fig. 5 demonstrates the impact of the UAV's altitude on the OSCP of the BIH and BIL. The figure reveals that there exists an ideal point of UAV's altitude h_U^* that maximizes the OSCP. This can be explained by the relation between LoS and NLoS propagation in the UAV-IDs reception. As the the UAV's altitude is increased, the probability of encountering LoS eventually surpasses the probability of NLoS. However, the higher h_U results in the greater pass-loss and consequently hinders the system performance.

Fig. 6 demonstrates the impact of the EH ratio η on the OSCP of the BIH and BIL. The observation indicates the existences of an optimal point EH ratio η^* that maximizes the OSCP outcomes. As the EH ratio is increased, IDs dedicate a greater time portion to harvest energy, which leads to less time spend on the offloading procedure. Conversely, when the EH ratio is decreased, IDs spend less time on the EH, which potentially limits the IDs energy availability for the efficient task-offloading, hence decreasing the OSCP performance.

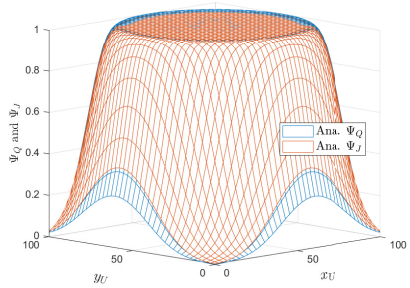

Fig. 7: Impact of the UAV's position (x_U, y_U) on OSCP of the BIH and BIL, with $Q = J = 20$, $\gamma_U = 2$ (dB), $h_U = 20$ (m), $\eta = 0.05$, $\Omega = 3$, and $\psi = 0.4$.

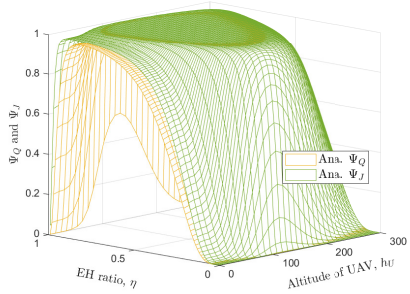

Fig. 8: Impact of the EH ratio and UAV's altitude on OSCP of the BIH and BIL, with $Q = J = 20$, $\gamma_U = 2$ (dB), $h_U = 20$ (m), $\eta = 0.05$, $\Omega = 3$, and $\psi = 0.4$.

Beyond optimizing UAV's altitude, determining the UAV's position plays a critical role in strengthening transmission links. Fig. 7 illustrates the impact of x_U and y_U on the OSCP value domains of the BIH and BIL. The figure reveals the existence of an optimal position (x_U^*, y_U^*) that maximizes OSCP outcomes. This observation aligns with the intuition that the UAV seeks a position that fosters the most favorable communication conditions.

Fig. 8 depicts the simultaneous impact of the EH ratio η and the UAV's altitude h_U on the OSCP of the BIH and BIL. By examining the combined impacts of the UAV's altitude in Fig. 5 and the EH ratio in Fig. 6, we can observed that there always exists the desirable (h_U^*, η^*) values to achieve the maximum OSCP values.

Fig. 9 and Fig. 10 illustrates the impact of the optimal values $(x_U^*, y_U^*, h_U^*, \eta^*)$ on OSCP of the BIH and BIL. We compare the optimal $(x_U^*, y_U^*, h_U^*, \eta^*)$ on OSCP of the BIH and BIL, illustrated in Table I, with the OSCPs of fixed (x_U, y_U, h_U, η) values. The results suggest that by utilizing **Algorithm 1**, the OSCP reach the maximum system offloading capability compared to the manually fixed points.

V. Conclusion

In this paper, we investigated an UAV-aided NOMA-MEC with WPT-enabled in IoT networks under Nakagami-m fad-

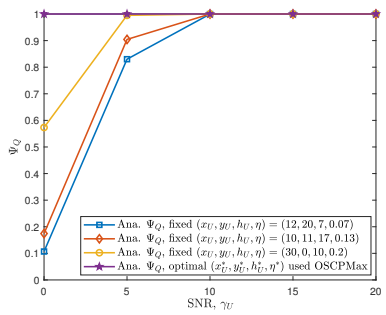

Fig. 9: Impact of the optimal $(x_U^*, y_U^*, h_U^*, \eta^*)$ on OSCP of the BIH, with $Q = J = 20$, and $\Omega = 3$.

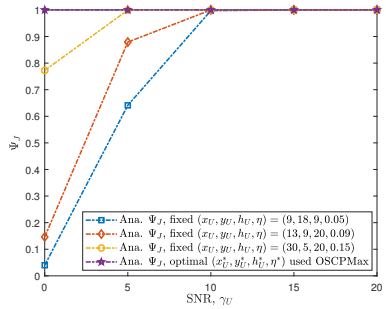

Fig. 10: Impact of the optimal $(x_U^*, y_U^*, h_U^*, \eta^*)$ on OSCP of the BIL, with $Q = J = 20$, $\Omega = 3$, and $\psi = 0.4$.

TABLE I: The optimal values of (x_U^*, y_U^*, h_U^*, η^*).

OSCP	γ_U	x_U^*	y_U^*	h_U^*	η^*
Ψ_Q	0	55.5655	67.7121	23.4155	0.4882
	5	66.2969	65.9549	16.4477	0.4460
	10	59.0496	59.0343	49.2009	0.6760
	15	49.6609	76.6213	28.8311	0.5350
	20	51.8605	65.4016	77.6963	0.3583
Ψ_J	0	53.1365	53.0137	4.1796	0.5086
	5	61.4928	56.8252	26.2012	0.3047
	10	47.2936	47.0318	22.6614	0.5635
	15	36.1517	23.3127	49.8151	0.4910
	20	44.7888	22.4136	127.0975	0.5849

ing channel. We presented a time-sequenced protocol for an efficient EH and offloading operation. The OSCP closed-form expressions were derived for the system efficacy assessments. To optimize OSCP, we presented a PSO-based solution that determines the UAV's positions and altitude, and the EH ratio. The Monte-Carlo findings were implemented to validate the offloading performance of the proposed system.

Appendix A.

By substituting (2), (3), (4), (5) into (6), we can express the Ψ_Q of the BIH as:

$$\Psi_Q = \left[\int_0^\infty f_y(y)\,dy - \int_0^\infty F_x\left(\Delta_Q^{(y)}\right) f_y(y)\,dy\right] \times \left[\int_0^\infty f_y(y)\,dy - \int_0^\infty F_x\left(\phi_Q^{(y)}\right) f_y(y)\,dy\right], \quad (8)$$

where $\Delta_Q^{(y)} = \sqrt{\frac{\delta_Q(z_2y^2+z_3)}{z_1}}$, $\phi_Q^{(y)} = \sqrt{\frac{\partial_Q(z_2y^2+z_3)}{z_1}}$. By substituting the PDF and CDF of the Nakagami-m distribution in (2) and (3), (8) can be rewritten as:

$$\Psi_Q = \left[\ddot{J}\sum_h (J-1)\,I_1 - \ddot{J}\sum_t (Q)\sum_l (J-1)\,I_2\right] \times \left[\ddot{J}\sum_h (J-1)\,I_1 - \ddot{J}\sum_p (Q)\sum_a (J-1)\,I_3\right], \quad (9)$$

where I_1, I_2, I_3 integrals are defined as:

$$I_1 = \int_0^\infty y^{m-1+\bar{h}} e^{-\frac{ym}{\xi_{j^*}}(h+1)} dy, \quad (10)$$

$$I_2 = \int_0^\infty \left(\Delta_Q^{(y)}\right)^{\bar{t}} e^{-\frac{tm}{\xi_{q^*}}\Delta_Q^{(y)}} y^{m-1+\bar{l}} e^{-\frac{ym}{\xi_{j^*}}(l+1)} dy, \quad (11)$$

$$I_3 = \int_0^\infty \left(\phi_Q^{(y)}\right)^{\bar{p}} e^{-\frac{pm}{\xi_{q^*}}\phi_Q^{(y)}} y^{m-1+\bar{a}} e^{-\frac{ym}{\xi_{j^*}}(a+1)} dy. \quad (12)$$

The I_1 integrals of (10) can be solved by adopting the Equation (3.351.3) in [12]. Furthermore, the I_2 and I_3 of (11), (12) can be solved with aid of the Gaussian-Chebyshev Quadrature formula from [13]. Thus, the closed-formed expression of the OSCP for the BIH is derived as in *Lemma 1*.

References

[1] J. Ji, K. Zhu, C. Yi, and D. Niyato, "Energy Consumption Minimization in UAV-Assisted Mobile-Edge Computing Systems: Joint Resource Allocation and Trajectory Design," IEEE Internet of Things Journal, pp. 8570-8584, 2021.

[2] A.-N. Nguyen, D.-B. Ha, T.-V. Truong, S. Sanguanpong, and C. So-In, "Secrecy Performance Analysis and Optimization for UAV-Relay-Enabled WPT and Cooperative NOMA MEC in IoT Networks," IEEE Access, pp. 127800-127816, 2023.

[3] X. Xu, H. Zhao, H. Yao, and S. Wang, "A Blockchain-Enabled Energy-Efficient Data Collection System for UAV-Assisted IoT," IEEE Internet of Things Journal, vol. 8, no. 4, pp. 2431-2443, 2021.

[4] A.-N. Nguyen et al., "UAV-aided uplink NOMA based on MEC in IoT networks: Secrecy offloading and Optimization," SaSeIoT, pp. 131-146, 2024.

[5] Ishan B., Neeraj K., Sudhanshu T., and Sudeep T., "Energy Consumption Minimization Scheme for NOMA-Based Mobile Edge Computation Networks Underlaying UAV," IEEE Systems Journal, vol. 15, no. 4, pp 5724-5733, 2021.

[6] X. Zhang et al., "Energy-Efficient Multi-UAV-Enabled Multiaccess Edge Computing Incorporating NOMA," IEEE Internet of Things Journal, vol. 7, no. 6, pp 5613-5627, 2021.

[7] R. Zhang et al., "Joint Location and Transmit Power Optimization for NOMA-UAV Networks via Updating Decoding Order," IEEE Wireless Communications Letters, vol. 10, no. 1, pp. 136-140, 2021.

[8] J. Men, J. Ge, and C. Zhang, "Performance Analysis for Downlink Relaying Aided Non-Orthogonal Multiple Access Networks With Imperfect CSI Over Nakagami-m Fading," IEEE Access, vol. 5, pp. 998-1004, 2016.

[9] B. Wang et al., "Optimal Altitude of UAV-BS for Minimum Boundary Outage Probability with Imperfect Channel State Information," in IEEE/CIC (ICCC), 2019.

[10] K. Dogbe and N. Hakem, "Analysis of full-duplex AF Relaying under Imperfect Channel State Information," in USNC-URSI, 2019.

[11] A.-N. Nguyen et al., "Performance Analysis and Optimization for IoT Mobile Edge Computing Networks With RF Energy Harvesting and UAV Relaying," IEEE Access, vol. 10, pp. 21526-21540, 2021.

[12] I Gradshteyn and I Ryzhik, Table of Integrals, Series, and Products. New York: Academic Press (Editor: A Jeffrey and D Zwillinger), 2014.

[13] K L Judd, "Quadrature Methods," University of Chicago's Initiative for Computational Economics (ICE).